PCCP

The Dimensional and Hydrogenating Effect on the Electronic Properties of ZnSe Nanomaterials: A Computational Investigation

Journal:	*Physical Chemistry Chemical Physics*
Manuscript ID	CP-ART-07-2018-004472.R1
Article Type:	Paper
Date Submitted by the Author:	31-Aug-2018

Complete List of Authors:	Lv, Xiaodong; Inner Mongolia University, Physical School of Science and Technology Li, Fengyu; Inner Mongolia University School of Physical Science and Technology, Gong, Jian; Inner Mongolia University Chen, Zhongfang; University of Puerto Rico, Department of Chemistry

The Dimensional and Hydrogenating Effect on the Electronic Properties of ZnSe Nanomaterials: A Computational Investigation

Xiaodong Lv,[1] Fengyu Li,[1,*] Jian Gong,[1,*] Zhongfang Chen[2,*]

[1] *Physical School of Science and Technology, Inner Mongolia University, Hohhot, China, 010021*

[2] *Department of Chemistry, The Institute for Functional Nanomaterials, University of Puerto Rico, Rio Piedras Campus, San Juan, PR 00931, USA*

*corresponding author: fengyuli@imu.edu.cn (FL); ndgong@imu.edu.cn (JG); zhongfangchen@gmail.com (ZC)

TOC

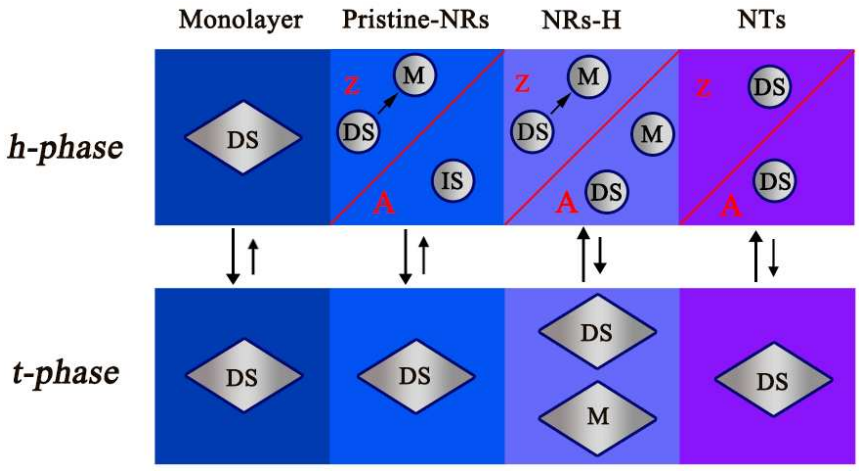

ABSTRACT

We performed a comprehensive first-principles study on the structural and electronic properties of ZnSe two-dimensional (2D) nanosheets and their derived one-dimensional (1D) nanoribbons (NRs) and nanotubes (NTs). Both hexagonal and tetragonal phases of ZnSe (h-ZnSe and t-ZnSe) were considered. The tetragonal phase is thermodynamically more favorable for 2D monolayer and 1D pristine ribbons, in contrast, the hexagonal phase is preferred for the edge-hydrogenated 1D NRs and NTs. The 2D h-ZnSe monolayer is a direct-bandgap semiconductor. Both the pristine zigzag nanoribbons (z-hNRs) and the corresponding edge-hydrogenated NRs gradually convert from direct-bandgap semiconducting phase into metallic phase as the ribbon width increases; the pristine armchair nanoribbons (a-hNRs) remain as semiconductors of indirect bandgaps with increasing ribbon width, and edge hydrogenating switches the indirect-bandgap feature to the direct-bandgap character or the metallic character as the different edge passivated style; the 1D h-ZnSe single-walled nanotubes in both armchair and zigzag forms keep the direct-bandgap semiconducting property of the 2D counterpart but with smaller band gaps. For the thermodynamically more favorable t-ZnSe monolayer, the intrinsic direct-bandgap semiconducting character is rather robust: The derived 1D nanoribbons with edge unsaturated or hydrogenated fully, and 1D single-walled nanotubes all preserve the direct-bandgap semiconducting feature. Our systemic study provides deep insights into the electronic properties of ZnSe-based nanomaterials and is helpful for experimentalists to design and fabricate ZnSe-based nanoelectronics.

KEYWORDS: ZnSe, two-dimension, one-dimension, nanosheet, nanoribbon, nanotube, stability, electronic structure, hydrogen passivation, density functional theory

1. INTRODUCTION

Since the discovery of graphene in 2004,[1] great progress has been achieved in the field of two-dimensional (2D) materials.[2,3] The 2D materials family has been continuously enriched by new family members, such as transition-metal dichalcogendies (TMDCs),[4] BN,[5] silicene,[6] germanane,[7] GaS,[8] phosphorene,[9] 2D transition metal carbides and nitrides with the chemical formula $M_{n+1}X_n$ (M = Sc, Ti, V, Cr, Zr, Nb, Mo, Hf, Ta; X = C, N; n = 1 – 3),[10] and various inorganic graphene analogues (IGAs).[11] Generally, these 2D nanomaterials are featured by high special surface area, abundant active surfaces, light in weight, high flexibility and transparency,[12] and have tunable electronic, optical, catalytic, and electrochemical properties, which bring great promise for modern technology.[13-24] For example, the single-layer MoS_2, the most famous member of TMDCs family, is a semiconductor with a direct band gap (~ 1.8 eV) and relatively high on/off ration, which is regarded as a promising material for field effect transistor.[25] Phosphorene, firstly isolated in the laboratory through mechanical exfoliation from bulk black phosphorus,[26] has the drain current modulation up to 10^5 and carrier mobility up to 1000 $cm^2 v^{-1} s^{-1}$, which makes it a potential candidate for future nanoelectronics applications.[9]

Among diverse 2D layered materials, group II-IV binary chalcogenides ZnX and CdX (X = S, Se, and Te) layered materials have drawn significant attentions in recent years.[40, 27 - 34] Due to the superior tunability in the electronic properties,[31] semiconductors ZnX and CdX have long been of tremendous interest for a board range of applications, including transistors, heterojunction diodes, photoconductors, and photovoltaic devices.[35-39] Recently, Sun *et al.* successfully synthesized the freestanding ZnSe monolayer with four-atom thickness and quasi-honeycomb lattice by using a strategy involving a lamellar hybrid intermediate, and their

photoelectrochemical tests demonstrated that this nanosheet has outstanding performance for solar water splitting.[40] This pioneering work inspired theoretical studies on the electronic structure and intrinsic properties of freestanding ZnSe monolayer, and various freestanding single-layer to multi-layer sheets of ZnX and CdX with or without honeycomb lattices have been proposed as synthesis targets.[28-33,41] Interestingly, a new structure of ZnSe monolayer with tetragonal lattice (t-ZnSe)[29,31] was predicted to be energetically more favorable than the experimentally synthesized pseudohexagonal ZnSe (ph-ZnSe) counterpart,[40] and might have superior incident photon-to-current conversation efficiency for solar water splitting.[29,31,32] Moreover, the electronic and optical properties of the doped t-ZnSe monolayer,[41,42] its potential applications in photocatalyst and Li-ion batteries,[43] and the photocatalytic properties of the tetragonal ZnS/ZnSe hetero-bilayer have also been theoretically investigated.[44]

Tunability of electronic properties of 2D materials is crucial for their applications in electronics and optoeletronics. Previous theoretical studies mainly focused on the structural properties and its applications in photocatalysis and energy storage of the 2D ZnSe sheets, but a few important issues related to ZnSe nanomaterials have not been addressed. For example, what are the stabilities of 1D ZnSe nanoribbons and nanotubes in hexagonal and tetragonal phases? How do the electronic characters of these 1D ZnSe nanomaterials vary compared to the 2D counterparts? In this article, we reported a systematic study of the stability of 1D ZnSe nanoribbons and single-walled ZnSe nanotubes, and compared their electronic properties to the 2D nanosheets. The computational results show that the dimensional effect is important to tune the electronic properties.

2. COMPUTATIONAL METHODS

In this work, all the computations were performed with the periodic density functional theory (DFT) with plane-wave basis set as implemented in the Vienna *ab initio* simulation package (VASP).[45-47] The ion-electron interaction was described with the projector augmented wave (PAW) method.[48] The Perdew-Burke-Ernzerhof (PBE)[49] functional under generalized gradient approximation was used to describe the exchange and correlation. The plane-wave basis set with the energy cutoff of 500 eV was used through all computations. Brillouin zone sampling was adopted with the Monkhorst-Pack (MP) special k-point meshes.[50] The k grids for nanosheet, nanoribbon, nanotube were 10×10×1, 1×10×1 and 1×1×10, respectively, for geometry optimizations. The vacuum space was larger than 10 Å between two adjacent images. Geometric structures were relaxed until the force on each atom is less than 1×10^{-4} eV/Å and the energy convergence criteria is 1×10^{-5} eV/Å. For every system, the unit cell was optimized to obtain the lattice parameters corresponding to the lowest energy. Considering the underestimated band gaps by PBE functional, the Heyd-Scuseria-Ernzerh hybrid functional (HSE06)[51,52] was used to get more reliable band gap values.

To evaluate the stabilities of ZnSe monolayers, nanoribbons and nanotubes, we calculated the cohesive energy per atom (E_c) using the following definition: $E_c = (nE_{Zn} + mE_{Se} - E_{ZnSe}) / (m + n)$, where E_{Zn}, E_{Se} and E_{ZnSe} represent the total energy of a Zn atom in bulk Zn, a Se atom in bulk Se, and the ZnSe per unitcell, respectively, n(m) denotes the number of Zn (Se) atoms in a unit cell. According to this definition, systems with larger values (positive) of E_c are energetically more favorable. For the edge-hydrogenated nanoribbons, the binding energy per H atom is defined as $E_b = (nE_H + E_{NR} - E_{H\text{-}NR}) / n$, where E_H, E_{NR}/$E_{H\text{-}NR}$, and n are the half energy of an isolated

H_2 molecule, total energy of pristine/hydrogenated ZnSe NRs, and the number of H atoms, respectively. On the basis of this definition, systems with stronger binding strengths have larger (positive) E_b.

3. RESULTS AND DISSCUSSION

3.1. The pristine two-dimensional ZnSe nanosheets.

We first studied the 2D ZnSe monolayers in hexagonal and tetragonal phases (Figure 1). The hexagonal structure (h-ZnSe) possesses Pmn21 symmetry (space group number 31), and the optimized lattice parameters are a = 3.97 Å and b = 5.85 Å. The orthogonal unit cell contains two Zn and two Se atoms, each Se (Zn) atom is surrounded by three Zn (Se) atoms. The nearest Se–Se and Zn–Se distances are 3.97 Å and 2.39 Å, respectively, which are close to the experimentally measured values (4.01 Å and 2.46 Å, respectively).[40] The hexagonal structure has four-atomic layers, each Zn atom is tricoordinated with three Se atoms, forming a buckled hexagonal networks with a thickness (d) of 2.38 Å (Figure 1a). The tetragonal phase (t-ZnSe) of ZnSe monolayer possesses P4/nmm symmetry (space group number 129), and the optimized lattice parameters are $a = b$ = 4.10 Å. The tetragonal unit cell contains two Zn atoms and two Se atoms, each Zn (Se) atom is tetracoordinated with four Se (Zn) atoms. The t-ZnSe monolayer has three atomic layers, forming a buckled tetragonal networks with a thickness (d) of 2.99 Å (Figure 1b). Note that both the h-ZnSe and t-ZnSe monolayers are buckled instead of planar structure, since the buckled surface can decrease the surface energy and then endow them enhanced stability.[40,53]

To compare their relative stabilities, we computed the cohesive energies of monolayer h-ZnSe and t-ZnSe, respectively. The cohesive energy of t-ZnSe (2.26 eV) is slightly larger than that of h-ZnSe (2.25 eV), which is in line with previous report

that the tetragonal structure is more stable.[29,31] The quite close cohesive energy of these two configurations of ZnSe monolayers simulates us to estimate the relative proportions. Based on Boltzmann's distribution, as demonstrated by the Boltzmann's factor (Figure S1), the t-ZnSe dominates monolayer structure at very low temperature, while as the temperature is higher than 50 K, both structures are in very similar probabilities.

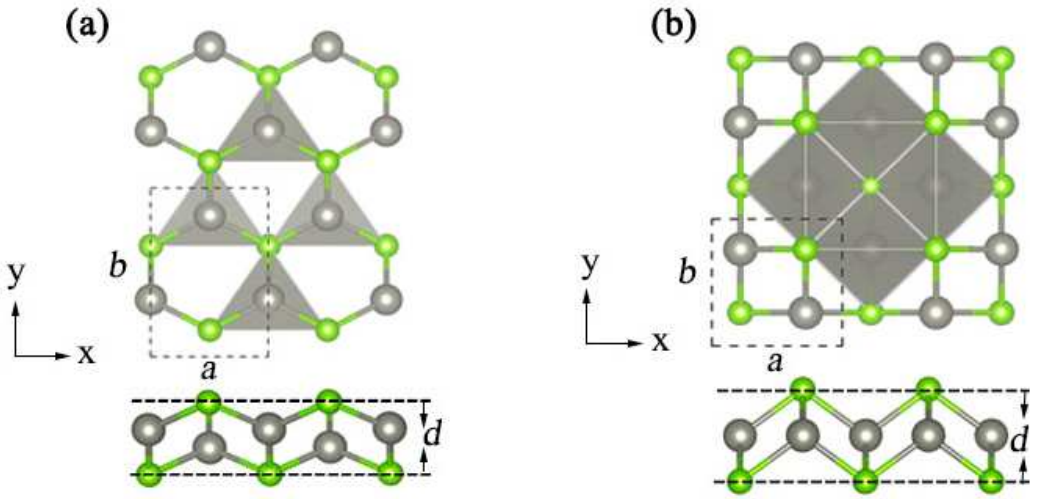

Figure 1. Top and side views of (a) the hexagonal ZnSe (h-ZnSe) and (b) the tetragonal ZnSe (t-ZnSe) monolayers. The green and gray spheres represent Se and Zn atoms, respectively. The unit cell of h-ZnSe and t-ZnSe monolayers are highlighted by the dashed rectangle and square, respectively. *a*, *b* and *d* represent the lattice parameters of unit cell in the axial direction and the thickness of monolayer ZnSe, respectively.

Then, we studied the electronic properties of these two ZnSe monolayers. Since the PBE functional tends to underestimate the band gaps, we also used the HSE06 functional for band structure calculations. If not specified, the results in the following are from PBE computations.

As shown in Figure 2(a), the h-ZnSe monolayer is a direct bandgap semiconductor. The PBE band gap is 2.34 eV, whereas the HSE06 value is about 3.40

eV, which is in good agreement with the experimental value (~ 3.50 eV).[31] The partial charge density distribution corresponding to the valence-band maximum (VBM) and conduction-band minimum (CBM) (Figure 2) indicates that both VBM and CBM are contributed by Se atoms, and mainly from Se *p* orbital. Because of the heteropolarity of the Zn-Se bonds, the electron-rich region is mainly near Se atoms. Similarly, the t-ZnSe monolayer also exhibits the semiconducting feature with a direct bandgap (2.11 and 3.30 eV, respectively, at PBE and HSE06 level of theory). The VBM state is localized at the Se atoms and mainly composed of the Se *p* orbital. For CBM, the state is localized at the Zn atoms and mainly composed of the Zn *s* orbital. To quantitatively estimate charge transfer between Zn atoms and Se atoms, Bader charge analysis[54,55] was performed. Our calculation results revealed that each Zn atom donates 0.69 and 0.70 *e* respectively to the neighboring Se atoms for the h-ZnSe and t-ZnSe monolayers, the computed electrons transfer is in line with the larger electronegativity of Se (2.55) than Zn (1.65).

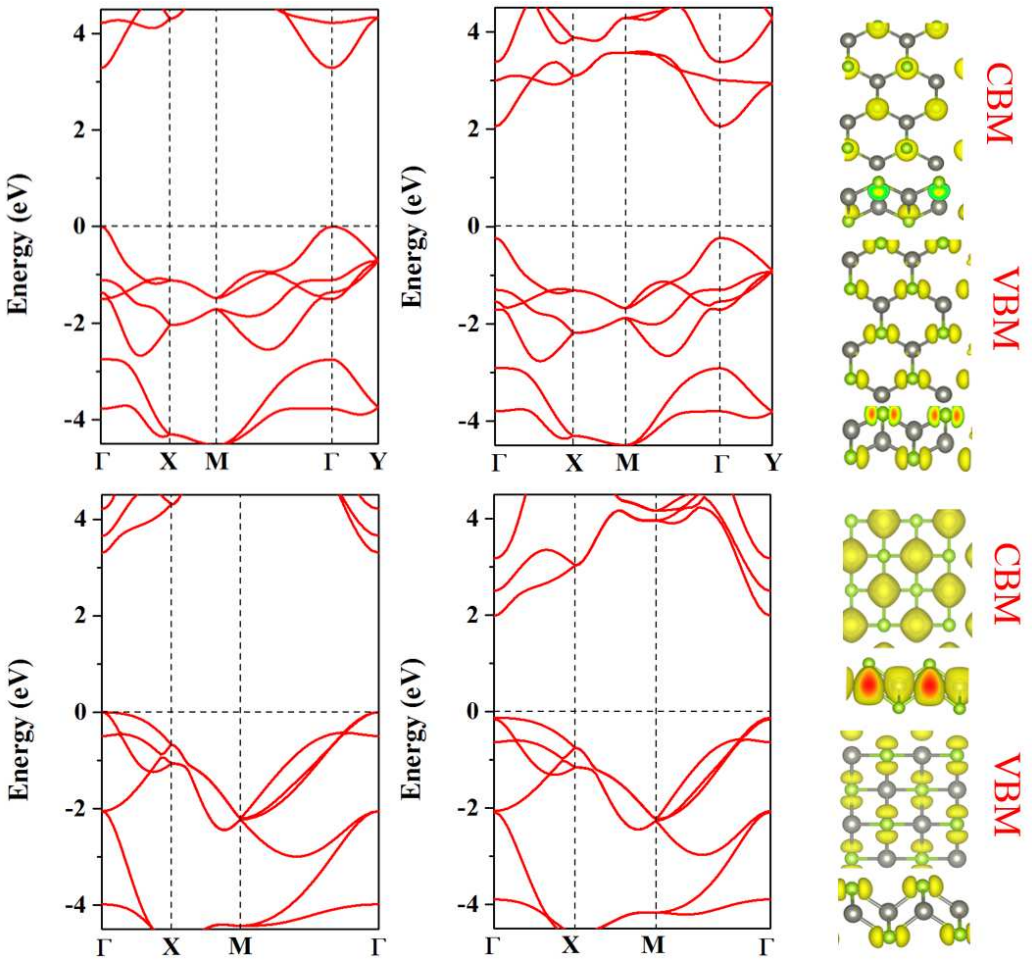

Figure 2. HSE06 (left panel) and PBE (middle panel) band structures of the monolayer (a) h-ZnSe and (b) t-ZnSe. The Fermi level is set to zero as indicated by the horizontal dashed lines. The right panels in Figure(a) and (b) show the partial charge density distributions of the valence band maximum (VBM) and the conduction band minimum (CBM), respectively. The isosurface value is 0.002e/Bohr^3. The green and gray spheres represent Se and Zn atoms, respectively.

3.2. The pristine one-dimensional ZnSe nanoribbons.

On the basis of the above work, we continued to investigate the derived nanoribbons. It is expected that the ZnSe nanoribbons can display even more interesting electronic properties. In the present work, two types of ZnSe nanoribbons, namely armchair (a-hNRs) and zigzag (z-hNRs), can be obtained by cutting the hexagonal ZnSe monolayer along *y*-axis and *x*-axis directions, respectively; however,

only one type of ZnSe nanoribbons of the ZnSe tetragonal monolayer can be obtained (tNRs). Here we considered N = 4 –17 (7.91 Å ~ 35.60 Å), 4 –16 (11.69 Å ~ 46.77 Å) and 4 –16 (8.21 Å ~ 32.82 Å) for a-hNRs, z-hNRs, and tNRs, respectively (N is the ribbon width). Figure 3a, b and c show the structures of a-13-hNR, z-10-hNR and 10-tNR with the ribbon width of 13, 10 and 10, respectively.

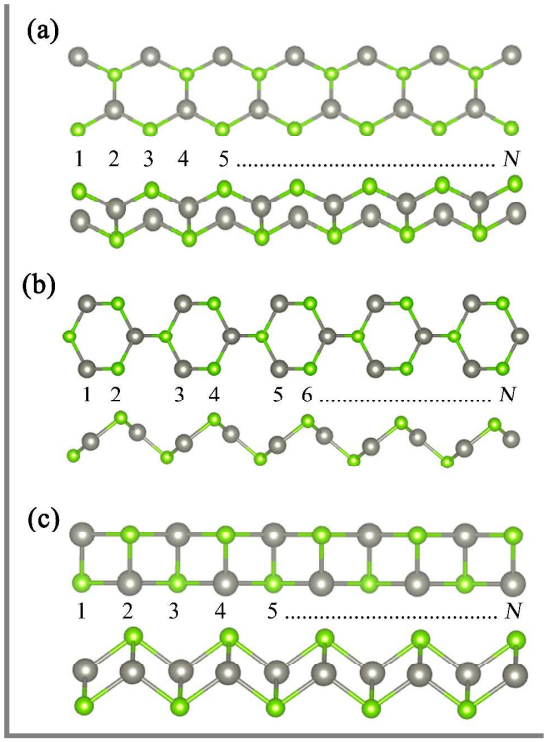

Figure 3. Structures of ZnSe nanoribbons with unpassivated edges (top and side views): (a) an armchair hexagonal ZnSe nanoribbon (a-hNRs), (b) a zigzag hexagonal ZnSe nanoribbon (z-hNRs) and (c) a tetragonal ZnSe nanoribbon (tNRs). N is the ribbon width. The green and gray spheres represent Se and Zn atoms, respectively.

Firstly, to examine the relative stabilities of these pristine ZnSe nanoribbons, we computed the cohesive energies for the a-hNRs, z-hNRs and tNRs versus the ribbon width N (see Figure 4c). Systems with greater E_c values are energetically more favorable according to the definition in computational method section. As discussed in section 3.1, the E_c of the t-ZnSe monolayer is slightly larger than that of the 2D

h-ZnSe. Expectantly, the cohesive energy of tNRs (E_c = 2.14~2.22 eV for N = 4–15) is larger than those of z-hNRs (E_c = 1.95~2.16 eV for N = 4–16) and a-hNR$_S$ (E_c = 2.06~2.19 eV for N = 4–17) with the same ribbon width N, indicating that the tNRs are thermodynamically more favorable. For the hNRs, armchair nanoribbons are energetically preferred since their E_c values are larger the zigzag ones of the same width N. The cohesive energy of the ZnSe nanoribbons increases gradually with increasing the ribbon width and gets close to the E_c of the 2D counterparts (Figure 4c). Experimentally, the 2D h-ZnSe has been synthesized,[10] and theoretically the 2D t-ZnSe was predicted to be more stable than h-ZnSe,[30] thus it is very promising to achieve the 1D h-ZnSe and t-ZnSe nanoribbons.

Next, we studied the electronic structure and width-dependent characteristics of the ZnSe nanoribbons. The electronic band structures and the partial charge density corresponding to the VBM and CBM of a-7-hNR and 7-tNR are shown in Figure 4a and 4b, which are representatives for the a-hNRs and tNRs, respectively. Our calculations revealed that the a-hNRs have an indirect bandgap character while the tNRs have a direct bandgap feature. Interestingly, with the increase of the ribbon width N, the electronic feature of z-hNRs can transfer from semiconductors with direct band gaps to metals when the ribbon width N reaches 7 (see Figure S2). For the a-hNRs, the VBM state is localized at the edges and mainly composes of the Se p orbital; the CBM state distributes inside the ribbon and is also mainly composing of the Se p orbital, together with some contribution from the Zn. However, for the tNRs, the VBM is contributed by p orbital of the non-marginal Se atoms, while the CBM is mainly contributed by the Zn atoms.

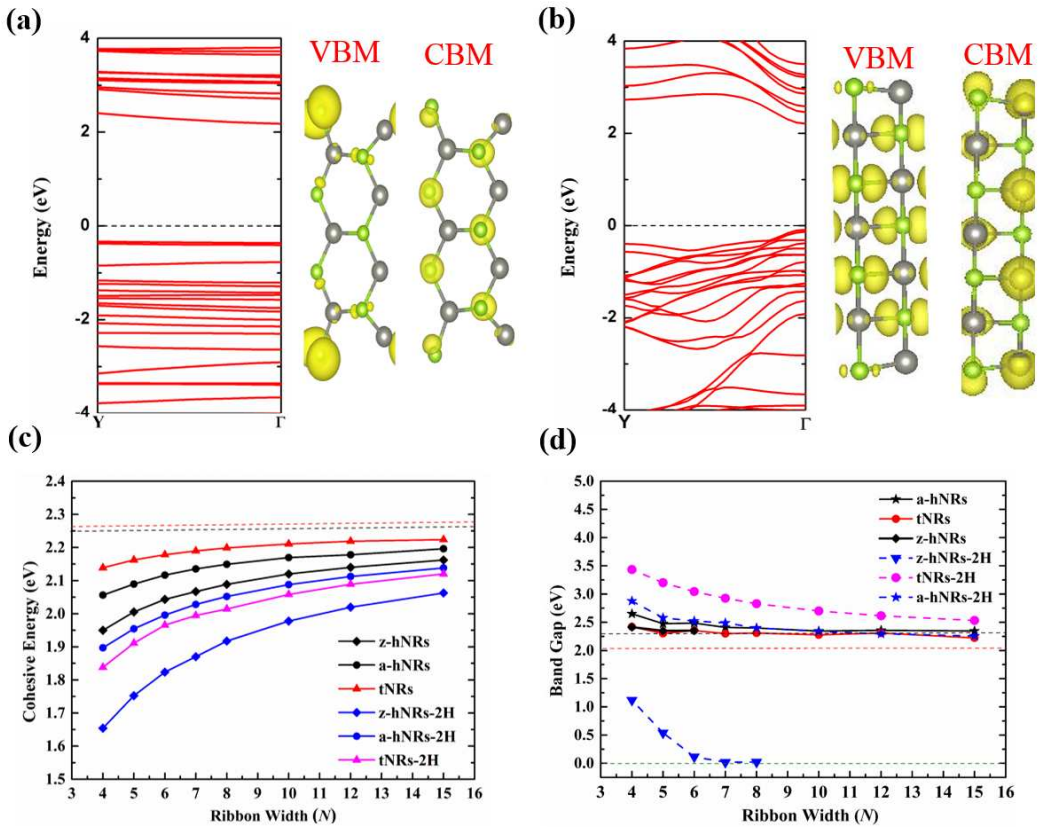

Figure 4. The computed band structures of the pristine a-7-hNR (a) and 7-tNR (b). The Fermi level is set to zero as indicated by the horizontal dashed lines. The right panels in (a) and (b) display partial charge density distribution corresponding to VBM and CBM. The isosurface value is 0.002e/Bohr^3. The green and gray spheres represent Se and Zn atoms, respectively. (c) The computed cohesive energies per atom of both the pristine ZnSe nanoribbons and the edge-hydrogenated ZnSe nanoribbons at both Zn and Se sites versus the ribbon width N. (d) The computed bandgaps of the pristine ZnSe nanoribbons and edge-hydrogenated ZnSe nanoribbons at both Zn and Se sites versus ribbon width N ($4 \leq N \leq 16$). The black and red dash lines in (c) and (d) represent the bandgap of monolayer ZnSe in tetragonal and hexagonal phase, respectively.

Furthermore, we investigated the variation of band gap of a-hNRs, z-hNRs and tNRs as a function of nanoribbons width N (Figure 4d). The band gap of the a-hNRs is larger than that of the tNRs at the same N (Figure 4d), which resembles the wider band gap of h-ZnSe monolayer compared with the t-ZnSe monolayer. For the a-hNRs

and tNRs, the band gap values generally decrease with local oscillations as the ribbon width *N* increases, and eventually when *N* approaches to infinity, the bandgap of the edge-unpassivated ZnSe NRs approaches to that of monolayer ZnSe (2.34 eV and 2.11 eV for hexagonal and tetragonal phases, respectively, at PBE level of theory). However, this expected convergence does not occur for the z-hNRs: when the ribbon width *N* reaches 7, z-hNRs become metallic. In order to explore the origin of the semiconductor-metal transition, we compared the structural characteristics and plotted the total density of states (TDOS) and local density of states (LDOS) of z-hNRs (see Figure S2, S3). Our computed results revealed that the initial z-hNRs structures with smaller ribbon width *N*, such as $N = 4, 5, 6$, are unstable and transform into analogous tNRs after structure optimizations and they have a direct bandgap characters, the VBM states mainly originate from the *p* orbitals of the non-margin Se atoms and the CBM states are mainly contributed by Zn *s* orbital; For the relatively larger ribbon width z-hNRs with $N \geqslant 7$, the structures retain the hexagonal feature, and the z-hNRs have metallic behaviors, we check that the metallic states across the Fermi level is mainly originate from the Se *p* orbital and Zn *s* orbital of inner atoms.

3.3. The edge-hydrogenated 1D ZnSe nanoribbons.

The edge atoms with dangling bonds significantly influence the electronic properties of pristine nanoribbons, the passivation of edge atoms such as hydrogen may bring significant changes to the properties of the nanoribbons.[56,57] Thus, besides the pristine ZnSe nanoribbons, i.e., the edge-unpassivated NRs, we also investigated the structural and electronic properties of the edge-hydrogenated ZnSe nanoribbons (NRs-H). From our test calculations, we found that the average binding energy of a hydrogen atom for a-7-hNR saturated at the edge Zn site is 1.99 eV, which is ~0.43

eV lower than that of the a-7-hNR saturated at the edge Se site (2.42 eV), indicating that the formation of Se−H bonds is more feasible than Zn−H bond formation. Previously, Tang *et al*. investigated the hydrogenation of Zn sites and O sites of ZnO nanosheets, respectively, and for a certain thickness of ZnO sheet, Zn is more liable to form bonds with H.[58] Providing that the hydrogen is excessive for hydrogenating Se edge atoms, the formation of Zn−H bonds is highly possible. Thus, two situations of edge hydrogenation were considered: the hydrogen saturation only at the Se edge sites (NR-1H), and the edge hydrogenation with both edge Se and Zn atoms (NR-2H). Nanoribbons with the width N = 4 – 16, 4 – 15, and 4 – 15 were chosen for a-*N*-hNRs-*n*H, z-*N*-hNRs-*n*H and *N*-tNRs-*n*H as representatives to investigate the different configuration edge hydrogenation effect, respectively, n represent the number of edge-hydrogenated sites (n = 1, 2 denotes the hydrogenation only at the edge Se site, and both edge Se and Zn atoms, respectively). Figure 5(a-f) represents the structures of a-15-hNR-*n*H, z-12-hNR-*n*H and 12-tNR-*n*H with the ribbon width of 15, 12 and 12, respectively. Clearly the edge atoms almost maintain the same configurations as in the 2D states.

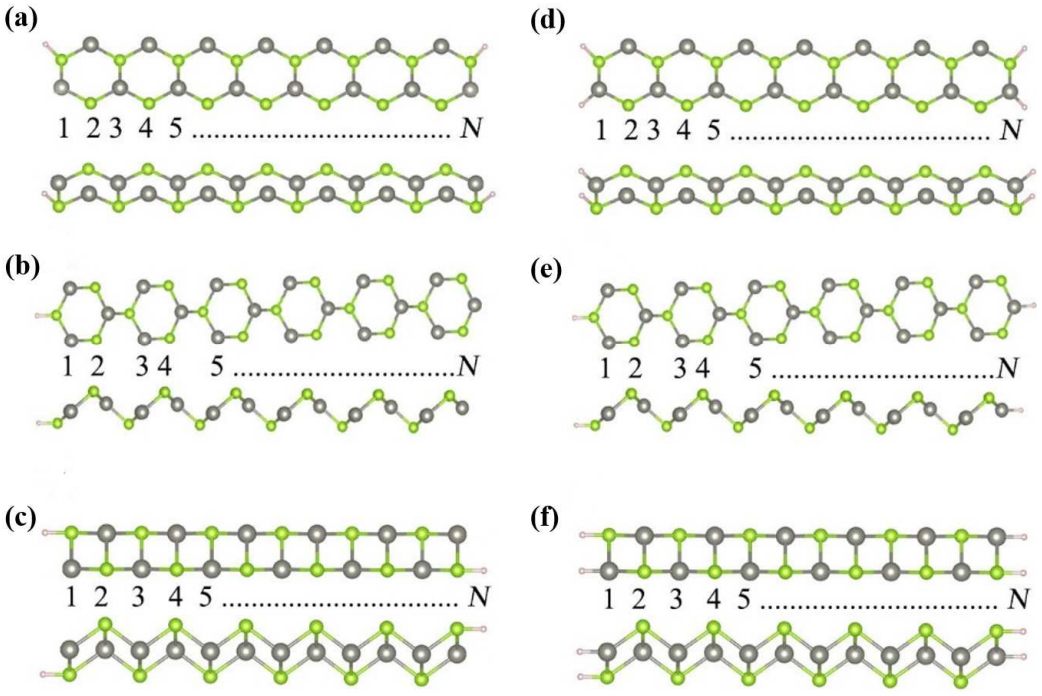

Figure 5. Top and side views (a) the armchair hexagonal ZnSe nanoribbon (a-15-hNR-1H), (b) the zigzag hexagonal ZnSe nanoribbon (z-12-hNR-1H), (c) the tetragonal ZnSe nanoribbon with edge hydrogenated (12-tNR-1H), (d) the armchair hexagonal ZnSe nanoribbon (a-15-hNR-2H), (e) the zigzag hexagonal ZnSe nanoribbon (z-12-hNR-2H) and (f) the tetragonal ZnSe nanoribbon with edge hydrogenated (12-tNR-2H), N is the ribbon width. The green, gray and white spheres represent Se, Zn and H atoms, respectively.

In terms of the structural stability, the binding energies per hydrogen atom of the edge-hydrogenated hNRs at both the edge Zn and Se sites are 2.10, 2.11, 0.76 and 0.76 eV, respectively, for a-8-hNR-2H, a-10-hNR-2H, z-8-hNR-2H and z-10-hNR-2H; the corresponding values are both 1.85 eV for 8-tNR-2H and 10-tNR-2H (see Figure S4). Thus, edge-hydrogenated a-hNRs-2H are energetically more preferable than a-hNRs-2H and tNRs-2H.

In order to further evaluate the relative stability, we calculated the cohesive energy per atom (E_c) using the following definition: $E_c = (nE_H + mE_{Zn} + zE_{Se} -$

$E_{H\text{-}ZnSe}$)/(n+m+z), where E_H, E_{Zn} and E_{Se} are the half energy of an isolated H_2 molecule, the total energy of a Zn atom in bulk Zn and a Se atom in bulk Se, respectively; $E_{H\text{-}ZnSe}$ is the total energy of hydrogenated ZnSe NRs, and *n, m* and *z* are the number of H, Zn and Se atoms in the ZnSe NRs supercell, respectively. According to this definition, systems with greater cohesive energy per atom are energetically more stable. For the edge-hydrogenated hNRs at only the edge Se sites, the cohesive energy of z-hNRs-1H (E_c = 1.96~2.17 eV for N = 4–15) is larger than those of a-hNRs-1H (E_c = 1.90~2.14 eV for N = 4–15) and tNRs-1H (E_c = 1.84~2.13 eV for N = 4–15) with the same ribbon width N (see Figure S5), indicating that the z-hNRs-1H are thermodynamically more favorable. For the ZnSe NRs with hydrogenation at both edge Se and Zn sites, the cohesive energy of a-hNRs-2H (E_c = 1.89~2.13 eV for N = 4–15) is larger than those of tNRs-2H (E_c = 1.83~2.12 eV for N = 4–15) and z-hNRs-2H (E_c = 1.65~2.06 eV for N = 4–15) with the same ribbon width N, that is, the a-hNRs-2H are also thermodynamically more favorable (see Figure 4c). These computed results are in line with the conclusion of previous binding energies compute.

The passivation of Zn and Se atoms at the edges by hydrogen atoms significantly affects the electronic properties. For the hydrogen passivated ZnSe nanoribbons only at the egde Se sites, we took the a-hNRs-1H, z-hNRs-1H and tNRs-1H with N = 7 as the prototype to explore the electronic properties. The three ribbons all exhibit metallic character (see Figure 6). We further investigated the variation of electronic properties of a-hNRs-1H, z-hNRs-1H and tNRs-1H as a nanoribbons width N (see Figure S6-S8), the Se-edge hydrogenated NRs are all metals independent with the ribbon width.

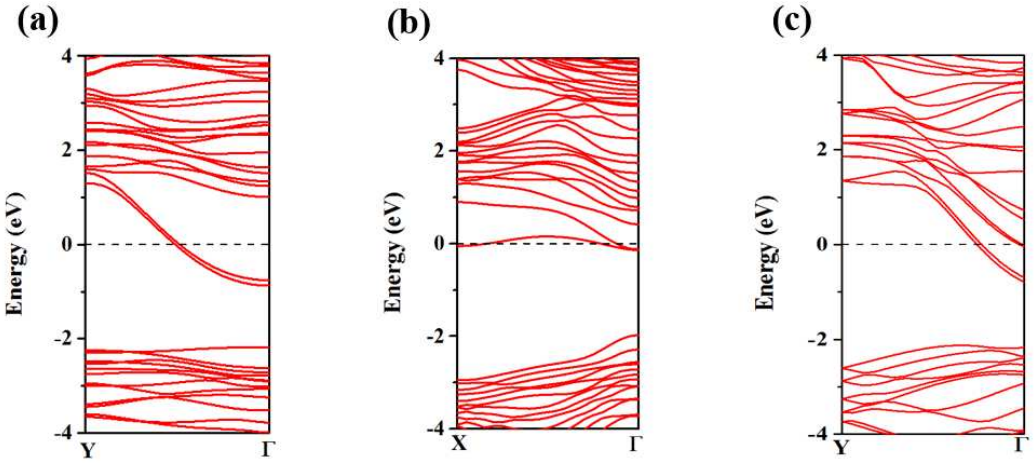

Figure 6. The computed band structures (PBE) of (a) the a-7-hNR-1H, (b) z-7-hNR-1H and (c) 7-tNR-1H. The Fermi level is set to zero as indicated by the horizontal dashed line.

Figure 4d summarizes the variation of the band gap for the hydrogen saturated ZnSe nanoribbons at both the edge Zn and Se sites as a function of ribbon width *N*. For the z-hNRs-2H, their band structures follow the same trend as those of pristine nanoribbons: the direct bandgap of z-hNRs-2H decreases as the ribbon width increases, and the bandgap almost becomes zero (a metal) at $N = 8$ (Figure 7a, b), the VBM and CBM are largely composed of the edge sides atoms. For the a-hNRs-2H, the indirect band-gap semiconductors are converted into direct band-gap semiconductors when the edge is passivated by hydrogen (Figure 7c), the VBM is mainly composed of Se *p* orbits while the CBM is distributed on the inner Se atoms. For the tNRs-2H, the edge passivation by hydrogen preserves the direct-bandgap semiconducting property of the pristine ribbons, the VBM and CBM in tNRs are mainly contributed by the Se *p* orbitals and Zn *s* orbitals of the inner atoms, respectively (Figure 6d), however, the bandgap values are markedly enlarged due to edge states (2.30 eV vs 2.93 eV). For both a-hNRs-2H and tNRs-2H, the band gaps are large at small *N*, but approach to those of 2D counterparts as the width *N*

increases, which can be easily understood by the quantum-size effect. At the same width, the band gap of a-hNR-2H is smaller than that of tNR-2H, which shows the opposite trend for the edge-unsaturated nanoribbons (see Figure 4d). By comparing Figure 7c,d and Figure 4a,b, we could figure out that the edge-hydrogenation alter the distributions of VBM and CBM, and further alter the band gaps of the edge-hydrogenated NRs.

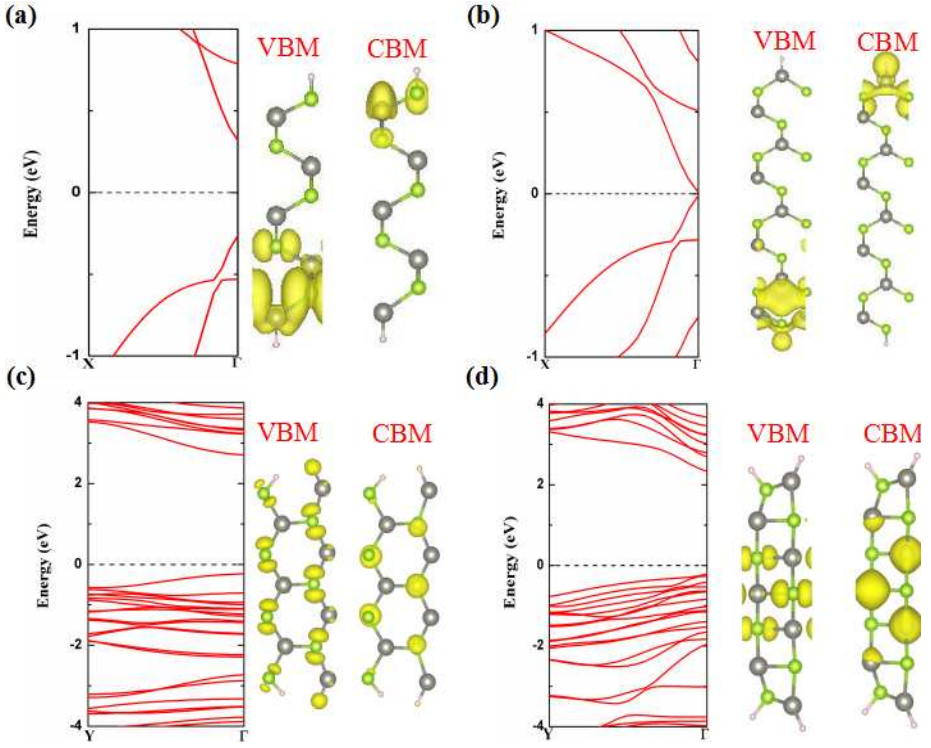

Figure 7. The computed band structures (PBE) of (a) the z-5-hNR-2H, (b) z-8-hNR-2H, (c) a-7-hNR-2H and (d) 7-tNR-2H. The corresponding partial charge density distributions of VBM and CBM are displayed in the right panels. The isosurface value is 0.003 e/Bohr^3. The Fermi level is set to zero as indicated by the horizontal dashed lines. The green and gray spheres represent Se and Zn atoms, respectively.

3.4. The one-dimensional single-walled ZnSe nanotubes.

A single-walled ZnSe nanotube can be viewed as rolling up a ZnSe nanosheet. Here three types of single-walled ZnSe nanotubes, namely, the armchair hexagonal

ZnSe nanotubes (a-hNTs), the zigzag hexagonal ZnSe nanotubes (z-hNTs) and the tetragonal ZnSe nanotubes (tNTs), can be obtained by rolling up ZnSe monolayers. The configuration of any specific single-walled ZnSe-NTs can be described with a pair of integer indexes (n_1, n_2).[59,60] Thus, there are three types of ZnSe nanotubes, namely z-hNTs, a-hNTs and tNTs, which are denoted as (n_1, 0), (n_1, n_2), and (0, n_2), respectively. In this work, we investigated the structural and electronic properties of single-walled ZnSe-NTs with small diameters in the range of 10 ~19 Å, for which (6, 6), (10, 0) and (0, 10) nanotubes were chosen to represent armchair nanotubes, zigzag nanotubes in hexagonal phase and nanotubes in tetragonal phase, respectively (Figure 8).

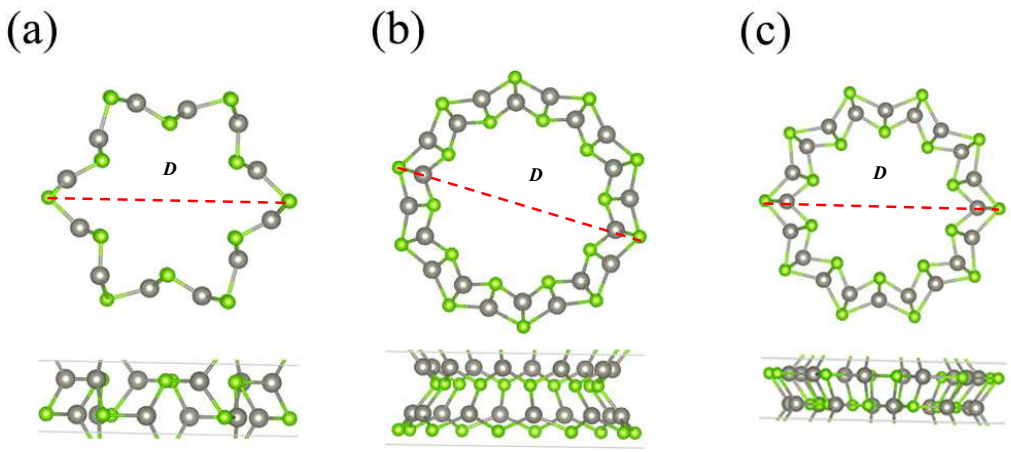

Figure 8. Top and side views of the optimized (a) a-hNT (6, 6), (b) z-hNT (10, 0) and (c) tNT (0, 10). *D* is the diameter of the ZnSe nanotubes. The green and gray spheres represent Se and Zn atoms, respectively.

After structure optimization, we found there is no obvious structural parameter change for the a-hNTs, including the diameter (*D*) of the nanotube and the length of the unit cell (L_c) in the axial direction (Table 1). The optimized L_c of the a-hNTs decreases slightly as the diameter increases (L_c = 3.97 Å for *D* = 11.17 Å, and L_c = 3.96 Å for *D* = 18.61 Å). However, we found the z-hNTs surface configuration occur reconstructions after geometry optimizations (see Figure S9), obviously, the tube wall

thicknesses of z-hNTs are thinner than that of pristine nanotubes, the atoms on the surface of the zigzag nanotube are arranged neatly to form a uniform plane and the L_c gradually increases with increasing D, from L_c = 6.88 Å for (8, 0) to L_c = 6.96 Å for (12, 0). Interestingly, for the tNTs with smaller diameters, such as (0, 8), (0, 9) and (0, 10), the initial tNTs structures transform into a-hNTs after structure optimizations, the length of the unit cell (L_c) in the axial direction is also 3.97 Å, independent with the increases of tube diameter; however, for tNTs with relatively larger diameter, such as (0, 11) and (0, 12), no obvious change in morphology was observed, and the tetragonal folded surface structure was maintained after structural relaxation, the length of the unit cell in the axial direction is almost independent with the diameters, showing the same trend as that of a-hNTs.

Table 1. The calculated diameters (D), length of the unit cell (L_c) in the axial direction, cohesive energy per atom (E_c), strain energy per atom (E_{str}), and bandgap (E_g) of ZnSe nanotubes (at PBE level of theory).

Models	D (Å)	L_c (Å)	E_c (eV)	E_{str} (eV)	E_g (eV)
(6, 6)	11.17	3.97	2.78	0.02	2.29
(7, 7)	13.03	3.97	2.79	0.01	2.30
(8, 8)	14.89	3.97	2.79	0.01	2.30
(9, 9)	16.76	3.97	2.80	0.00	2.31
(10, 10)	18.61	3.96	2.80	0.00	2.31
(8, 0)	10.10	6.88	2.78	0.03	2.16
(9, 0)	11.13	6.90	2.77	0.03	2.12
(10, 0)	12.63	6.92	2.77	0.03	2.11
(11, 0)	13.87	6.94	2.77	0.03	2.08
(12, 0)	15.15	6.96	2.77	0.03	2.06
(0, 8)	10.45	3.97	2.79	0.02	2.31
(0, 9)	13.06	3.97	2.79	0.02	2.31
(0, 10)	14.37	3.97	2.79	0.02	2.32
(0, 11)	15.68	4.13	2.70	0.11	1.12
(0, 12)	16.98	4.13	2.72	0.09	1.20

In order to evaluate relative stabilities of ZnSe nanotubes, we calculated the cohesive energy per atom and strain energy per atom (E_{str}), respectively. The strain

energy per atom was defined as the difference of the cohesive energy per atom between a perfect ZnSe monolayer and the ZnSe nanotube. The E_{str} values of a-hNTs, z-hNTs and tNTs with different tube diameters are presented in Table 1. Note that nanotubes with smaller strain energies per atom are energetically more favorable. As expected, the strain energy decreases with the increasing D. We found that a-hNTs have lower E_{str} than that of z-hNTs and tNTs with similar diameters, implying the a-hNTs are more stable than z-hNTs and tNTs. For comparison, we also calculated the strain energies of the armchair (a-MoS_2-NTs) and zigzag (z-MoS_2-NTs) MoS_2 nanotubes (see Table S1) with the similar diameters. The strain energies of ZnSe NTs are much smaller than those of the MoS_2 NTs. The in-plane stiffness of a 2D sheet is a key factor to the magnitude of strain energy of the nanotubar derivates.[61] We computed the in-plane stiffness of h-ZnSe and t-ZnSe, as well as the MoS_2 monolayer. The computed in-plane stiffness of the monolayer h-ZnSe (40.99 N/m) and t-ZnSe (40.81 N/m) are much smaller than that of the MoS_2 monolayer (129.55 N/m), suggesting the ZnSe monolayer are much less rigid than the MoS_2 monolayer, and as a results, the ZnSe nanotubes have low strain energies than MoS_2 nanotubes.

We further explored the electronic properties of the ZnSe nanotubes, for which the band structures of (10, 0), (6, 6), (0, 10) and (0, 11) nanotubes were chosen as representatives for the z-hNTs, a-hNTs and tNTs, respectively (Figure 9). All these types of nanotubes are direct-bandgap semiconductors, both VBM and CBM are located at the Γ point, and are mainly contributed by Se atoms (Figure 9). The band gap values of these nanotubes are all smaller than their 2D counterparts (2.34 eV and 2.11 eV for hexagonal and tetragonal phase, respectively). Rolling the hexagonal monolayer into armchair or zigzag nanotubes results in slight decrease of band gaps, in contrast, a dramatic reduction of the band gap values occurs for the larger diameter

tetragonal phase (tNTs). For the armchair hNTs, the bandgap is almost independent with the diameter, the bandgap increases from 2.29 eV for D = 11.17 Å to 2.31 eV for D = 18.61 Å; for the zigzag hNTs, the bandgap decreases gradually from 2.16 eV for D = 10.10 Å to 2.06 eV for D = 15.15 Å. However, for the relative smaller (0, 8), (0, 9) and (0, 10) tNTs, because of the structural transition, the electronic structures are the same with a-hNTs, which keeps direct band-gap semiconducting feature, and the bandgaps are also independent with the diameter; while for the relatively larger diameter tNTs, the bandgaps are smaller than a-hNTs and z-hNTs, but the bandgap increases markedly with increasing the tube diameters (from E_g = 1.12 eV for D = 15.68 Å to E_g = 1.20 eV for D = 16.98 Å).

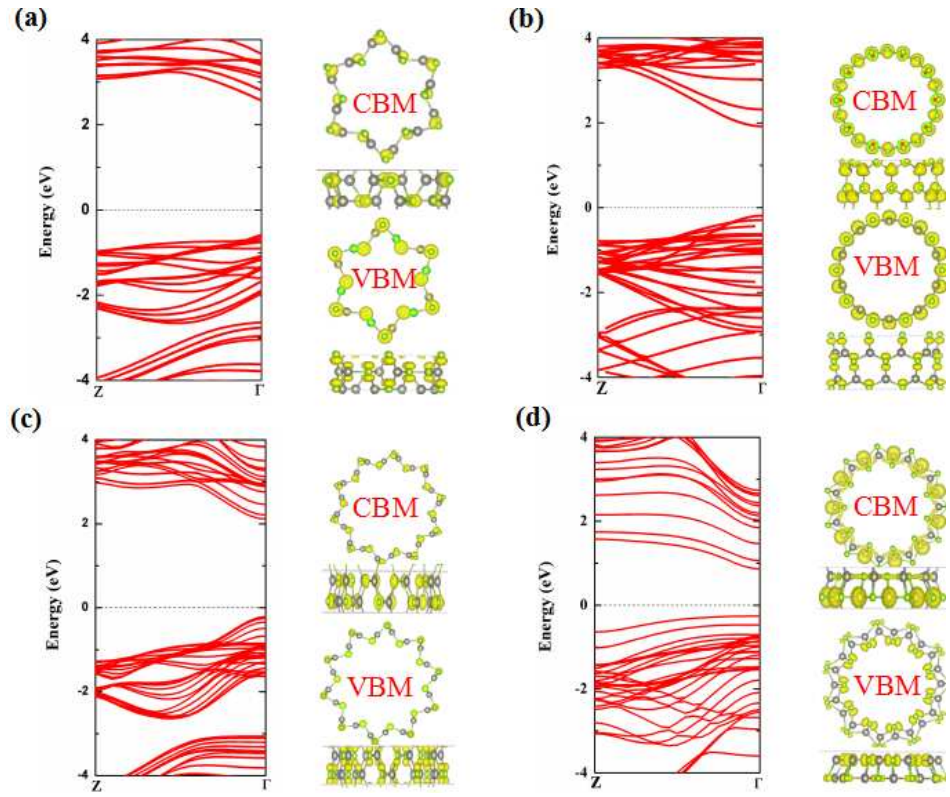

Figure 9. Band structure (PBE) and the corresponding partial charge density distributions of VBM (bottom panel) and CBM (up panel) of (a) armchair (6, 6), (b) zigzag (10, 0) hNTs and (c) (0, 10), (d) (0, 11) tNTs. The Fermi level is set to zero as indicated by the horizontal dashed lines. The isosurface value is 0.003e/Bohr^3. The green and gray spheres represent Se and Zn atoms, respectively.

4. CONCLUSION

In this work, we presented a detailed DFT study on the structural and electronic properties of 2D ZnSe nanosheets, and the derived 1D nanoribbons and nanotubes in both *h*-phase and *t*-phase. Our computations show that the tetragonal monolayer is slightly more stable than the hexagonal counterpart, and both monolayers are direct-bandgap semiconductors. Cutting the 2D nanosheets into 1D nanoribbons, the resulting NRs in tetragonal phase (tNRs) also have higher stability compared to those in hexagonal phase (hNRs). The tNRs are found to be direct band gap semiconductors and the relatively more stable a-hNRs exhibit the indirect-bandgap semiconductor feature, while the less stable z-hNRs can be direct-bandgap semiconductors or metals depending on the ribbon width. When the edge is saturated by hydrogen atoms at the Zn and Se edge sites, the a-hNRs-2H become more stable than the tNRs-2H. The tNRs-2H are still direct-bandgap semiconductors; the a-hNRs-2H restore the original direct-bandgap semiconductor character as the 2D counterpart is. However, when only the edge Se sites is saturated by hydrogen atoms, the z-hNRs-1H become more stable than the tNRs-1H, the a-hNRs-1H, z-hNRs-1H and tNRs-1H are all exhibit metallic character. When folding the 1D nanoribbons into 1D single-walled nanotubes, the a-hNTs are also more stable than z-hNTs and even more stable than the tNTs, all these NTs are direct-bandgap semiconductors with smaller gap values than their 2D counterparts. For clarity, all these above finding are summarized in Figure 10.

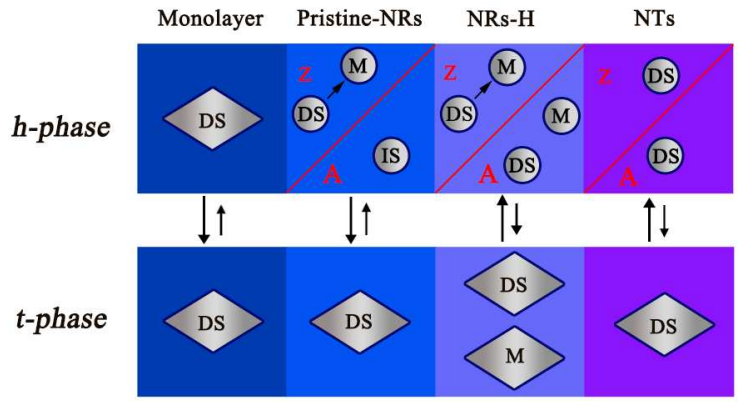

Figure 10. The relative stabilities and electronic properties of the ZnSe monolayer, pristine nanoribbons, edge-hydrogenated nanoribbons (NRs-H), and nanotubes (NTs) in *h*-phase and *t*-phase. DS, IS and M denote the direct-bandgap semiconductors, indirect-bandgap semiconductors and metals, respectively. For the 1D derivatives, the larger Z/A, means higher stabilities for zigzag/armchair nanoribbons/nanotubes.

The ZnSe monolayers in tetragonal and hexagonal phases are both kinetically stable as demonstrated by all positive frequencies in the calculated phonon spectra.[9,29] Moreover, Li *et al*. Born-Oppenheimer molecular dynamic simulations revealed that at the fixed pressure of 700 MPa, the hexagonal ZnSe monolayer can be easily transformed to the tetragonal structure.[9] We further investigated the thermodynamic stabilities of h-ZnSe and t-ZnSe via first-principles molecular dynamic (FPMD) simulations at 300 K. Both ph-ZnSe and t-ZnSe can well keep their original structures through a 8 ps of FPMD simulation at 300 K, indicating the high stabilities of monolayer ZnSe, and after full atomic relaxation, the final h-ZnSe and t-ZnSe structures of FPMD simulations can easily recover their initial configurations (Figure S10). These results suggest that both h-ZnSe and t-ZnSe have good thermodynamic stabilities. Since the hexagonal ZnSe monolayer was successfully obtained in Xie's group [*Nat. Commun.*, 2012, **3**, 1], the tetragonal ZnSe monolayer is highly possible

to be fabricated. By cutting and rolling the 2D monolayer, the 1D nanoribbons and single-walled nanotubes could be realized, respectively.

Our study provides deep understanding into the electronic properties of the ZnSe-based nanomaterials, and offers a simple and effective route to tune the electronic behavior of ZnSe nanostructures. Moreover, the recently synthesized 47 TMC compounds and heterostructures,[62] makes us very optimistic to experimentally achieve those ZnSe-based nanomaterials.

ACKNOWLEDGEMENT

This work was supported in China by the National Nature Science Foundation of China (No.11464032) and Startup Project of Inner Mongolia University, and in USA by NSF-CREST Center for Innovation, Research and Education in Environmental Nanotechnology (CIRE2N) (Grant Number HRD-1736093).

REFERENCES

(1) A. K. Geim, K. S. Novoselov, The rise of graphene, *Nat. Mater*., 2007, **6**(3), 183–192.

(2) Q. Tang, Z. Zhou, Graphene-analogous low-dimensional materials, *Prog. Mater. Sci*., 2013, **58**(8), 1244–1316.

(3) Q. Tang, Z. Zhou and Z. F. Chen, Innovation and discovery of graphene-like materials via density-functions theory computations, *Comput. Mol. Sci.*, 2015, **5**(5), 360–379.

(4) S. Manzeli, D. Ovchinnikov, D. Pasquier, O. V. Yazyev and A. Kis, 2D transition metal dichalcogenides, *Nat. Rev. Mater.*, 2017, **2**(8), 1–15.

(5) K. Watanabe, T. Taniguchi and H. Kanda, Direct-bandgap properties and evidence for ultraviolet lasing of hexagonal boron nitride single crystal, *Nat. Mater.*, 2004, **3**(6), 404–409.

(6) P. Vogt, P. De. Padova, C. Quaresima, J. Avila, E. Frantzeskakis, M. C. Asensio,

Resta, B. Ealet and G. Le Lay, Silicene: compelling experimental evidence for graphene like two-dimensional silicon, *Phys. Rev. Lett.*, 2012, **108**(15), 155501.

(7) E. Bianco, S. Butler, S. Jiang, O. D. Restrepo, W. Windl and J. E. Goldberger, Stability and exfoliation of germanane: a germanium graphene analogue, *ACS Nano*, 2013, **7**(5), 4414–4421.

(8) D. J. Late, B. Liu, H. S. S. R. Matte, C. N. R. Rao and V. P. Dravid, Rapid characterization of ultrathin layers of chalcogenides on SiO_2/Si substrates, *Adv. Funct. Mater.*, 2012, **22**(9), 1894–1905.

(9) L. Li, Y. Yu, G. J. Ye, Q. Ge, X. Ou, H. Wu, D. Feng, X. H. Chen and Y. Zhang, Black phosphorus field-effect transistors, *Nat. Nanotechnol.*, 2014, **9**(5), 372–376.

(10) M. Naguib, V. N. Mochalin, M. W. Barsoum and Y. Gogotsi, MXene: a new family of two-dimensional materials, *Adv. Mater.*, 2014, **26**(7), 992–1005.

(11) C. N. R. Rao, H. S. S. Ramakrishna Matte and U. Maitra, Graphene analogues of inorganic layered materials, *Angew. Chem. Int. Ed.*, 2013, **52**(50), 13162–13185.

(12) H. W. Zhu and M. Wang, Two-dimensional materials: structure, preparation and properties, *J. Chin. Ceram. Soc.*, 2017, **45**(8), 1043–1053.

(13) A. Kara, H. Enriquez, A. P. Seitsonen, L. C. Lew Yan Voon, S. Vizzini, B. Aufray and H. Oughaddou, A review on silicene–new candidate for electronics, *Surf. Sci. Rep.*, 2012, **67**(1), 1–18.

(14) A. J. Mannix, B. Kiraly, M. C. Hersam and N. P. Guisinger, Synthesis and chemistry of elemental 2D materials, *Nat. Rev. Chem.*, 2017, **1**, 1–14.

(15) C. L. Tang and H. Zhang, Two-dimensional transition metal dichalcogenide nanosheet-based composites, *Chem. Soc. Rev.*, 2015, **44**(9), 2713–2731.

(16) L. Liu, J. Zhang, J. Zhao and F. Liu, Mechanical properties of graphene oxides, *Nanoscale*, 2012, **4**(19), 5910–5916.

(17) X. Li and H. W. Zhu, Two-dimensional MoS_2: properties, preparation, and applications, *J. Mater.*, 2015, **1**(1), 33–44.

(18) C. Y. Zhi, Y. Bando, C. C. Tang, H. Kuwahara and D. Golberg, Large-scale fabrication of boron nitride nanosheets and their utilization polymeric composites with improved thermal and mechanical properties, *Adv. Mater.*, 2009, **21**(28), 2889–2893.

(19) G. Wang, X. G. Zhu, Y. Y. Sun, Y. Y. Li, T. Zhang, J. Wen, X. Chen, K. He, L. L. Wang, X. C. Ma, J. F. Jia, S. B. Zhang and Q. K. Xue, Topological insulator thin films

of Bi_2Te_3 with controlled electronic structure, *Adv. Mater.*, 2011, **23**(26), 2929–2932.

(20) C. Tan, X. Cao, X. Wu, Q. He, J. Yang, X. Zhang, J. Chen, W. Zhao, S. Han, G. W. H. Nam, M.Sindoro and H. Zhang, Recent advances in ultrathin two-dimensional nanomaterials, *Chem. Rev.*, 2017, **117**(9), 6225–6331.

(21) N. A. Kumar, M. A. Dar, R. Gul and J. B. Baek, Graphene and molybdenum disulfide hybrids: synthesis and applications, *Mater. Today*, 2015, **18**(5), 286–298.

(22) M. Pumera and Z. Sofer, 2D monoelemental arsenene, antimonene, and bismuthene: beyond black phosphorus, *Adv. Mater.*, 2017, **29**(21), 1–8.

(23) J. H. Shen, Y. H. Zhu, H. Jiang and C. Z. Li, 2D nanosheets-based novel architectures: synthesis, assembly and applications, *Nano Today*, 2016, **11**(4), 483–592.

(24) J. Zhu, E. Ha, G. L. Zhao, Y. Zhou, D. Huang, G. Z. Yue, L. S. Hu, N Sun, Y. Wang, L. Y. S. Lee, C. Xu, K. Y. Wong, D. Astruc and P. X. Zhao, Recent advance in MXenes: a promising 2D materials for catalysis, sensor and chemical and adsorption, *Coord Chem. Rev.*, 2017, **352**, 306–327.

(25) B. Radisavljevic, A. Radenovic, J. Brivio, V. Giacometti and A. Kis, Single-layer MoS_2 transistors, *Nat. Nanotechnol.*, *2*011, **6**(3), 147–150.

(26) A. Castellanos-Gomez, L. Vicarelli, E. Prada, J. Q. Island, K. Narasimha -Acharya, S. I. Blanter, D. J. Groenendijk, M. Buscema, G. A. Steele and J. Alvarez, "Isolation and characterization of few-layer black phosphorus," *2D Mater.*, 2014, **1**(2), 1−19.

(27) S. Z. Karazhanov, P. Ravindran, A. Kjekshus, H. Fjellvag and B. G. Svensson, Electronic structure and optical properties of ZnX (X = O, S, Se, Te): a density functional study, *Phys. Rev. B*, *Condens. Matter*, 2007, **75**(15), 155104.

(28) J. Zhou, J. Huang, B. G. Sumpter, P. R. C. Kent, H. Terrones and S. C. Smith, Structures, energetics, and electronic properties of layered materials and nanotubes of cadmium chalcogenides, *J. Phys. Chem. C*, 2013, **117**(48), 25817−25825.

(29) C. J. Tong, H. Zhang, Y. N. Zhang, H. Liu and L. M. Liu, New manifold two-dimensional single-layer structures of zinc-blende compounds, *J. Mater. Chem. A*, 2014, **2**(42), 17971−17978.

(30) J. Zhou, J. Huang, B. G. Sumpter, P. R. C. Kent, Y. Xie, H. Terrones and S. C. Smith, Theoretically predictions of freestanding honeycomb sheets of cadmium chalcogenides, *J. Phys. Chem. C*, 2014, **118**(29), 16236−16245.

(31) L. Li, P. Li, N. Lu, J. Dai and X. C. Zeng, Simulation evidence of hexagonal–to –tetragonal ZnSe structures transition: a monolayer material with a wide-range tunable direct bandgap, *Adv. Sci.*, 2015, **2**(12), 1500290.

(32) J. Zhou, B. G. Sumpter, B. R. C. Kent and J. Huang, A novel and functional single-layer sheet of ZnSe, *ACS Appl. Mater. Interfaces*, 2015, **7**(3), 1458−1464.

(33) J. Zhou, Y. Li, X. Wu and W. Qin, Modulating the electronic and optical properties of tetragonal ZnSe monolayer by chalcogen dopants, *ChemPhysChem*, 2016, **17**(13), 1993−1998.

(34) X.-D. Wen, R. Hoffmann and N. W. Ashcroft, Two-dimensional CdSe nanosheets and their interaction with stabilizing ligands, *Adv. Mater.*, 2013, **25**(2), 261 −266.

(35) S. Ithurria, M. D. Tessier, B. Mahler, R. P. S. M. Lobo, B. Dubertret and A. L. Efros, Colloiddal nanoplatelets with two-dimensional electronic structure, *Nat. Mater.*, 2011, **10**(12), 936−941.

(36) S. Ithurria and B. Dubertret, Quasi 2D colloidal CdSe platelets with thicknesses controlled at the atomic level, *J. Am. Chem. Soc.*, 2008, **130**(49), 16504−16505.

(37) J. S. Son, X. D. Wen, J. Joo, J. Chae, S. i. Baek, K. Park, J. H. Kim, K. An, J. H. Yu, S. G. Kwon, S. H. Choi, Z. W. Wang, Y. W. Kim, Y. Kuk, R. Hoffmann and T. Hyeon, Large-scale soft colloidal template synthesis of 1.4 nm thick CdSe nanosheets, *Angew. Chem., Int. Ed.*, 2009, **48**(37), 6861−6864.

(38) S. Ithurria, G. Bousquet and B. Dubertret, Continuous transition from 3D to 1D confinement observed during the formation of CdSe nanoplatelets, *J. Am. Chem. Soc.*, 2011, **133**(9), 3070−3077.

(39) Z. Li and X. Peng, Size/Shape-controlled synthesis of colloidal CdSe quantum disks: ligand and temperature effects, *J. Am. Chem. Soc.*, 2011, **133**(17), 6578−6586.

(40) Y. Sun, Z. Sun, S. Gao, H. Cheng, Q. Liu, J. Piao, T. Yao, C. Wu, S. Hu, S. Wei and Y. Xie, Fabrication of flexible and freestanding zinc chalcogenide single layers, *Nat. Commun.*, 2012, **3**, 1–7.

(41) J. Zhou and X. Wu, Alloy engineering of electronic and optical properties of tetragonal monolayer zinc chalcogenides, *J. Alloys Compd.*, 2017, **695**, 1392–1396.

(42) J. Zhou and X. H. Wu, First-principle study on doping of tetragonal ZnSe monolayers, *Mater. Today Chem.*, 2017, **4**, 40−44.

(43) J. Zhou, H. Zhuang and H. Wang, Layered tetragonal zinc chalcogenides for energy related applications: from photocatalysts for water splitting to cathode

materials for Li-Ion batteries, *Nanoscale*, 2017, **9**(44), 17303–17311.

(44) J. Zhou and X. Zhen, A theoretical perspective of the enhanced photocatalytic properties achieved by forming tetragonal ZnS/ZnSe hetero-bilayer, *Phys. Chem. Chem. Phys.*, 2018, **20**(15), 9950–9956.

(45) G. Kresse and J. Hafner, Ab initio molecular dynamics for liquid-metal-amorphous-semiconductor transition in germanium, *J. Phys. Rev. B*, 1994, **49**(20),14251−14269.

(46) G. Kresse and J. Hafner, Ab initio molecular dynamics for liquid metals, *Phys. Rev. B*, 1993, **47**(1), 558−561.

(47) K. Albe and J. Furthmüller, Efficient iterative schemes for ab initio total-energy calculations using a plane-wave basis set, *Phys. Rev. B*, 1996, **54**(16), 11169−11186.

(48) P. E. Blöchl, Projector augmented-wave method, *Phys. Rev. B*, 1994, **50**(24), 17953−17979.

(49) J. P. Perdew, K. Burke and M. Ernzerhof, Generalized gradient approximation made simple, *Phys. Rev. Lett*., 1996, **77**(18), 3865−3868.

(50) H. J. Monkhorst and J. D. Pack, Special points for brillouin-zone integrations, *Phys. Rev. B*, 1976, **13**(12), 5188−5192.

(51) J. Heyd, G. E. Scuseria and M. Ernzerhof, Hybrid functionals based on a screened coulomb potential, *J. Chem. Phys.*, 2003, **118**(18), 8207−8215.

(52) A.V. Krukau, O. A. Vydrov, A. F. Izmaylov and G. E. Scuseria, Influence of the exchange screening parameter on the performance of screened hybrid functionals, *J. Chem. Phys.*, 2006, **125**, 224106.

(53) C. Mcginley, M. Riedler and T. Möller, Evidence for surface reconstruction on InAs nanocrystals, *Phys. Rev. B*, 2002, **65**, 2453308.

(54) R. F. Bader, Atoms in molecules [M], Wiley Online Library, 1990.

(55) G. Henkelman, A. Arnaldsson and H. Jonsson, A fast and robust algorithm for bader decomposition of charge density, *Comput. Mater. Sci.*, 2006, **36**(3), 354−360.

(56) X. L. Ding, G. T. Yu,* X. R. Huang and W. Chen,* The donor/acceptor edge-modification: an effective strategy to modulate the electronic and magnetic behaviors of zigzag silicon carbon nanoribbons, *Phys. Chem. Chem. Phys.*, 2013, **15**(41), 18039−18047.

(57) W. Chen, H. Zhang, X. L. Ding, G. T. Yu,* D. Liu and X. R. Huang, Dihalogen edge-modification: an effective approach to realize the half-metallicity and metallicity

in zigzag silicon carbon nanoribbons, *J. Mater. Chem. C*, 2014, **2**(37), 7836−7850.

(58) Q. Tang, Y. F. Li, Z. Zhou, Y. S. Chen and Z. F. Cheng, Tuning electronic and magnetic properties of wurtzite ZnO nanosheets by surface hydrogenation, *ACS Appl. Mater. Interfaces*, 2010, **2**(8), 2442−2447

(59) (a) R. Tenne, M. Remškar, A. Enyashin and G. Seifert, Inorganic nanotubes and fullerene-like structures (IF). In: A. Jorio, G. Dresselhaus and M. S. Dresselhaus (eds) Carbon Nanotubes. Topics in applied physics, 111 (2007) 631−671. Springer, Berlin, Heidelberg. (b) M. S. Dresselhaus and P. Avouris, Introduction to carbon materials research. In: Dresselhaus M.S., Dresselhaus G., Avouris P. (eds) Carbon Nanotubes. Topics in applied physics, 80 (2001) 1–9. Springer, Berlin, Heidelberg.

(60) I. R. Shein, A. N. Enyashin, A. L. Ivanovskii, Nanotubes of layered iron-based superconductors: simulations of atomic structure and electronic properties. *Comp. Mater. Sci*., 2011, **50**(3), 824–827.

(61) D. H. Hodges, A. Rajagopal, J. C. Ho and W. Yu, Stress and strain recovery for the in-plane deformation of an isotropic tapered strip-beam. *J. Mech. Mater. Struct.*, 2010, **5**(6), 963−975.

(62) J. Zhou, J. Lin, X. Huang, Y. Zhou, Y. Chen, J. Xia, H. Wang, Y. Xie, H. Yu, J. Lei, F. Liu, Q. Zeng, C.-H, Hsu, C. Yang, L. Liu, T. Yu, Z. Shen, H. Lin, B. I. Yakobson, K. Suenaga, G. Liu and Z. Liu, A library of atomically thin metal chalcogenides, *Nature*, 2018, **556**(7701), 355−362.